Sweet spot of energy-level alignment in hyperfluorescent organic light-emitting diodes

Rishabh Saxena,[1,2,*,†] Giacomo Cotelli,[1,3,*] Kleitos Stavrou,[4] Engin Torun,[3] Larissa G. Franca,[4] Andrew P. Monkman,[4] Stefano Gottardi,[3] and Anna Köhler[1,‡]

[1] *Soft matter Optoelectronics, University of Bayreuth, Bayreuth, Germany*

[2] *Max Planck Institute for Polymer Research, Mainz, Germany*

[3] *Simbeyond B.V., Eindhoven, Netherlands*

[4] *Department of Physics, Durham University, Durham, UK*

(Received 18 March 2025; revised 22 May 2025; accepted 18 July 2025; published 26 August 2025)

We investigate loss mechanisms in hyperfluorescent organic light-emitting diodes (HF-OLEDs) with the emissive layer consisting of a host, a thermally activated delayed fluorescence (TADF) sensitizer, and a terminal emitter. We focus on understanding how the relative energy levels between the TADF sensitizer and terminal emitter impact device efficiency and roll-off through the formation and subsequent dissociation of an intermolecular state. Using a combined experimental and kinetic Monte Carlo (KMC) simulation-based approach, we analyzed HF-OLEDs incorporating either multiresonant (MR) or fluorescent (non-MR) terminal emitters. We find that selecting terminal emitters with ionization potential and electron affinity values that position the intermolecular state at least 150 meV above the singlet energy of the terminal emitter effectively suppresses the losses due to exciton dissociation. Furthermore, we show that using the MR emitter, which exhibits reverse intersystem crossing (RISC), significantly reduces residual triplet-related losses compared with the non-MR emitter. This further mitigates exciton dissociation losses, thereby improving the external quantum efficiency (EQE). These findings provide clear guidelines for selecting terminal emitters and optimizing energy level alignment to address intermolecular state-related loss pathways in HF-OLEDs.

DOI: 10.1103/k967-sr56

I. INTRODUCTION

Organic light-emitting diodes (OLEDs) have played a crucial role in transforming the display technology owing to their remarkable attributes such as high efficiency, flexibility, and potential for cost-effective manufacturing. Achieving high efficiency in OLEDs requires utilizing both singlet and triplet excitons. One approach involves using phosphorescent emitters, which incorporate heavy metals [1]. However, a heavy metal-free alternative is the use of thermally activated delayed fluorescence (TADF) emitters. This approach, pioneered by Adachi and coworkers, enables the efficient conversion of triplet excitons to singlet states through thermal activation, resulting in subsequent emission [2]. Although the first TADF emitters were organometallic complexes [3,4], subsequent developments have focused on purely organic TADF emitters. Despite their promising features, TADF emitters still face some challenges. They produce broad emission spectra, which compromise the color purity of OLEDs. For efficient TADF, the emitter must have a small energy gap between the lowest singlet and triplet states. This small gap can be achieved by reducing the overlap of electron and hole wave functions, which results in a charge-transfer (CT) character of the lowest energy singlet and triplet excited states. Unfortunately, the CT nature inherently implies broader emission spectra [5,6].

Initially investigated in standalone TADF OLED configurations, these emitters have now found novel applications in hyperfluorescent OLEDs (HF-OLEDs) [7]. In HF-OLEDs, the emissive layer (EML) typically consists of a host matrix, a TADF sensitizer, and a fluorescent terminal emitter. This composition facilitates efficient energy transfer of excitons generated on the TADF sensitizer to the fluorescent emitters [7,8]. The synergistic combination of TADF and fluorescence mechanisms takes advantage

*These authors contributed equally to this work

†Contact author: saxenar@mpip-mainz.mpg.de

‡Contact author: anna.koehler@uni-bayreuth.de

of the high triplet harvesting efficiency characteristic of the TADF sensitizer materials, coupled with the narrower emission spectra and enhanced operational lifetime provided by fluorescent emitters [7,9]. However, it has been noted that HF-OLEDs utilizing fluorescent terminal emitters often exhibit lower external quantum efficiency (EQE) compared with identical OLEDs without the terminal emitters [10,11]. This raises the question of what causes these efficiency losses and how to engineer the energy levels of the terminal emitter to prevent them.

There have been suggestions that loss processes associated with triplet states on the terminal emitter may contribute to the poor performance of some HF-OLEDs [5,12,13]. To address this, it was proposed to replace the commonly used fluorescent terminal emitter with an emitter that converts triplets to singlets via a TADF mechanism, while maintaining a narrow emission spectrum. This can be achieved using multiresonant (MR) emitters, which have a narrow emission spectrum due to their rigidity and a CT character resulting from a very short-range translation of the electron and hole wave functions [6]. Although this approach has produced some highly efficient OLEDs [14–16], there are instances where the use of MR emitters did not improve device efficiency and roll-off [13,16,17]. Stavrou *et al*. have also shown that the precise photophysical parameters, such as radiative lifetimes and intersystem crossing rate, of the TADF sensitizer play a critical role in the achievable EQE increase and its resistance to roll-off in MR-TADF-based hyperfluorescent OLEDs [16]. In our work, we perform a combined experimental and modeling study to understand how MR emitters might further improve device performance and, in particular, what energy level requirements are necessary for this improvement. We found that two conditions must be met. First, the ionization potential (IP) and electron affinity (EA) of the TADF sensitizer and the terminal emitter need to be designed such that any possible intermolecular state, such as an intermolecular charge-transfer state or an exciplex, between the TADF sensitizer and the terminal emitter would be higher in energy than the lowest energy singlet excited state of the terminal emitter. Second, the terminal emitter must have efficient reverse intersystem crossing (RISC) to eliminate any remaining triplets from the device.

There are two limiting cases when two chromophores are so close that their electronic systems interact. When the two chromophores have very distinct electron affinities, so that a full charge transfer takes place, the wave function of the resulting state will have significant ionic contributions and the state is referred to as a charge-transfer (CT) state. Conversely, for chromophores with similar electron affinities, only partial charge transfer may occur and, thus, covalent contributions from resonance interaction dominate. The species is called an exciplex [18], though this terminology is not always strictly adhered to, given the continuous transition between the two limits. Here, we are not concerned with the nature of any intermolecular state but with its energy and, henceforth, refer to it simply as the intermolecular state (IS). Thus, a central element in our study is designing the relative alignment of the energy levels of the TADF sensitizer and the terminal emitter. In principle, the IP and EA of the TADF sensitizer and terminal emitter may be nested, similar to energy level alignment prevailing in a type-I heterojunction architecture that promotes Förster-type resonance energy transfer (FRET). They can also be offset from each other, resembling the alignment known from a type-II heterojunction architecture that is conducive to the formation of an intermolecular state (Fig. 1).

To motivate our choice of materials, we briefly recall the advantages and disadvantages of each sensitizer-terminal emitter alignment. With a type-I-like alignment, the terminal emitter serves as a trap for both holes and electrons so that trap-assisted recombination of charges results in (nonemissive) triplet generation on the terminal emitter. This constitutes a significant efficiency loss process in type-I architecture-based HF-OLEDs [5,19], unless MR emitters are used as terminal emitters and employed at very low concentrations [20]. Furthermore, it allows for FRET, yet precludes significant charge-transfer interaction (Fig. 1). In contrast, a type-II-like alignment allows for charge-transfer interactions with the formation of an intermolecular state. Since the terminal emitter acts as a trap for either holes or electrons, but not both, direct recombination and, hence, exciton generation on the terminal emitter can be avoided, though at the expense of creating a charge recombination site. Hence, one solution is to use a type-II-like alignment but to aim for a minimal population of the intermolecular state formed between the TADF sensitizer and terminal emitter. For this, it is important to consider the energy of the intermolecular state. It was already recognized in the late 90s that the energy of an intermolecular state between two molecules may—in theory—be lower or higher than the singlet state energies of either molecule, yet a higher energy intermolecular state would not be stable, if it forms at all [21]. When the intermolecular state energy is lower than the singlet energy of the terminal emitter ("type-II-L" in Fig. 1), it will become populated instead of the terminal emitter's singlet state and may subsequently dissociate [22]. This is a well-recognized issue, exploited in the working principle of organic solar cells [18,21]. While the dissociation of excited states is, in principle, a known efficiency loss mechanism for OLEDs [22–25], its impact on the efficiency of hyperfluorescent OLEDS is not yet fully understood nor appreciated [21–25]. Moreover, the subsequent recombination of dissociated charges can increase triplet accumulation on the terminal emitter, further reducing OLED efficiency and worsening roll-off.

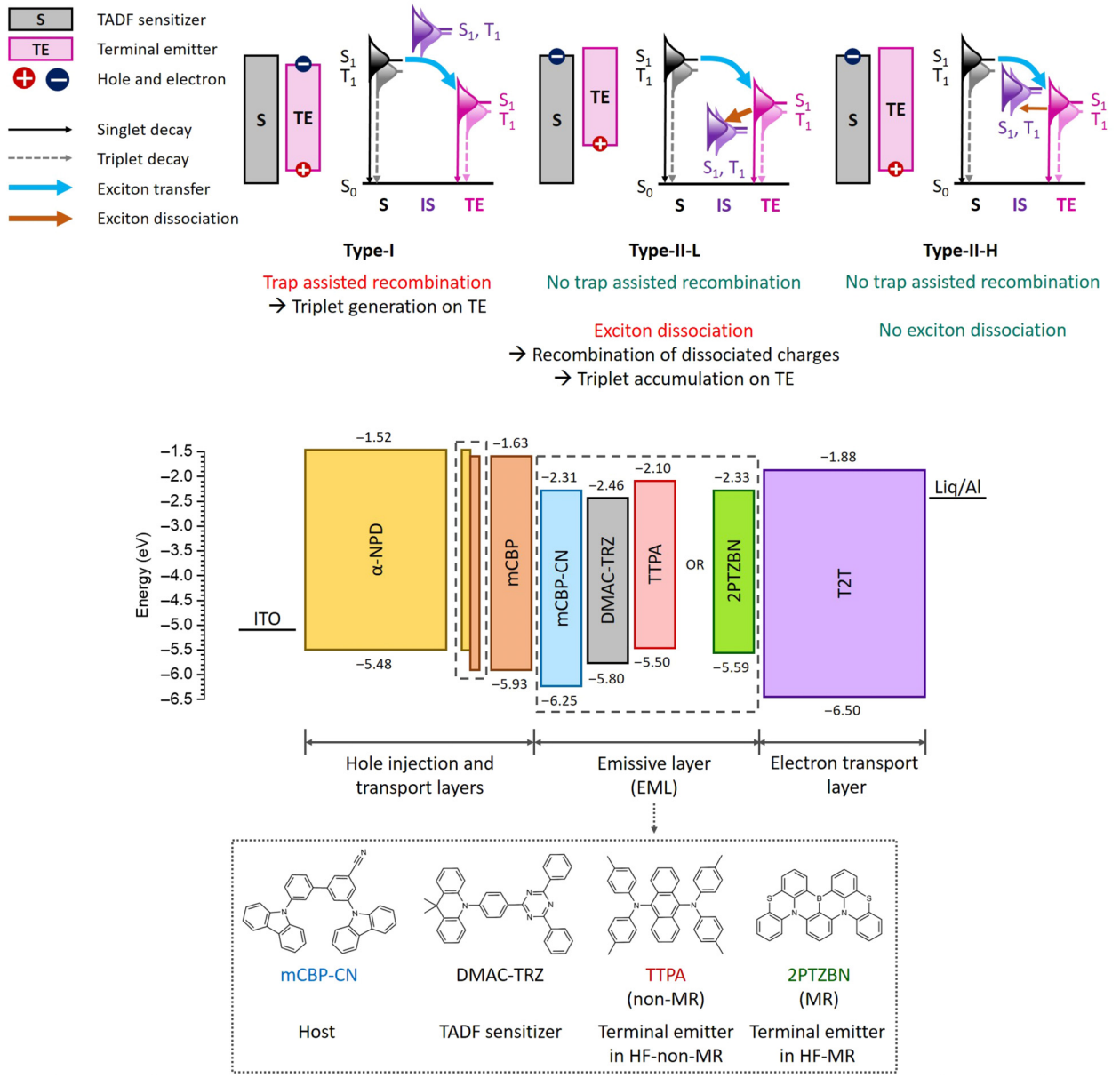

FIG. 1. OLED architecture and materials. (top) Energy level diagrams and Jablonski diagrams for type-I, II-L, and II-H heterojunction-like alignments between the TADF sensitizer and terminal emitter. (middle) Layer structure of the OLEDs studied in this work. Within the emissive layer, mCBP-CN is used as the host matrix and DMAC-TRZ is either used as an emitter (in ref-TADF OLEDs) or as a sensitizer (in HF-OLEDs). In HF-non-MR OLEDs, the non-MR fluorescent emitter TTPA acts as the terminal emitter whereas, in HF-MR OLEDs, the MR emitter 2PTZBN acts as the terminal emitter. Refer to Table II for more details on the device nomenclature and emissive layer composition. (bottom) Chemical structures of mCBP-CN, DMAC-TRZ, TTPA, and 2PTZBN are shown.

One promising approach to address this issue lies in fine tuning the energy of the intermolecular state by chemical design (i.e., modifying the IP and EA values of the molecules) such that an intermolecular state would be higher than the singlet energy of the terminal emitter ("type-II-H" in Fig. 1). This adjustment can effectively prevent (or minimize) exciton dissociation by transforming the occupation of the intermolecular state into a thermally activated process. This aspect has not yet been systematically studied in HF-OLEDs. Therefore, the key question in our study is whether such HF-OLEDs can be engineered by modifying the IP and EA values suitably. If so, what specific requirements regarding energy level alignment and terminal emitter properties need to be considered when designing such OLEDs to effectively suppress exciton dissociation?

II. METHODS

A. Experimental procedures

The materials used are as follows: N,N-bis(naphthalene-1-yl)- N,-bis(phenyl)benzidine (α-NPD), 3,3′-Di(9H-carbazol-9 yl)-1,1′-biphenyl (mCBP), 3,3′-di(carbazol-9-yl)-5-cyano-1,1′-biphenyl (mCBP-CN), 10-(4-(4,6 Diphenyl-1,3,5-triazin-2-yl)phenyl)-9,9-dimethyl-9,10-dihydroacridine (DMAC-TRZ), 9,10 Bis[N,N -di-(p-tolyl)-amino]anthracene (TTPA), [1,4] benzothiazino[4″, 3″,2″:1′,8′] [1,4]benzazaborino[4′,3′,2′:4,5] [1,4] benzazaborino [3,2,1 kl] phenothiazine (2PTZBN), 2,4,6-tris (biphenyl-3-yl)-1,3,5-triazine (T2T), 8 hydroxyquinolinolato-lithium (Liq), dipyrazino[2,3-f:2′,3′-h] quinoxaline-2,3,6,7,10,11 hexacarbonitrile (HAT-CN) and aluminum (Al). α-NPD, mCBP, and T2T were purchased from Sigma-Aldrich, while mCBP-CN was purchased from Ossila and sublimed before use. Sublimed DMAC-TRZ, TTPA, and 2PTZBN were purchased from Lumtec and were used as received.

The devices were fabricated on patterned indium tin oxide (ITO) coated glass substrates ($2.5 \times 2.5 \times 0.1$ cm) with a sheet resistance of 15 Ω/sq (VisionTek Systems). The substrates were cleaned by sonication in acetone and isopropanol, followed by oxygen plasma treatment. Subsequently, the cleaned substrates were placed in a deposition chamber (Kurt J. Lesker Super Spectros), where both the small molecule and cathode layers were thermally evaporated under vacuum pressures lower than 10^{-7} mbar. The device areas were either 4 or 8 mm^2.

The OLEDs were fabricated with the following configuration: ITO/α-NPD (35 nm)/mCBP: α-NPD (1:1, 5 nm)/mCBP (10 nm)/EML (25 nm)/T2T (40 nm)/Liq (3 nm)/Al (100 nm). For the symmetric electron-only device, the emissive layer is sandwiched between the well-known electron transport material T2T, with the device configuration: ITO/Liq (3 nm)/T2T (40 nm)/EML (25 nm)/T2T (40 nm)/Liq (3 nm)/Al (100 nm). Symmetric hole-only devices were fabricated with the configuration: ITO/α-NPD (35 nm)/mCBP: α-NPD (1:1, 5 nm)/mCBP (10 nm)/EML (25 nm)/mCBP (10 nm)/mCBP: α-NPD (1:1, 5 nm)/α-NPD (35 nm)/HAT-CN (10 nm)/Al (100 nm). HAT-CN was introduced in hole-only devices to block the injection of electrons from the cathode into the EML.

The devices were transferred into a calibrated 6-inch integrating sphere (Labsphere) within the glovebox. Electrical properties were assessed using a Keithley 2400 source meter. For the OLEDs, the emission spectra were recorded simultaneously using a calibrated fiber-coupled spectrometer (Ocean Optics USB4000) and a photodiode for low luminance measurements. All the evaluations were conducted at room temperature under a nitrogen atmosphere.

The thin film samples were kept in a continuous flow He-cryostat with a temperature controller. The samples were excited at 355 nm by a Q-switched laser from QS laser (MPL15100-DP). Emission from the samples was directed onto a spectrograph (Oriel MS257) and detected using a gated iCCD camera (iStar A-DH334T-18F-03). The measurements were conducted under vacuum (10^{-5} mbar) or in a He-filled atmosphere. Fluorescence and phosphorescence spectra were recorded at low temperatures (either 5 K or 77 K). The time-resolved PL measurements of the thin films were performed with exponentially increasing delay and gating times, with the gating time set to be 10 times lower compared with the delay time. The photoluminescence quantum yield of the thin film samples was measured in a N_2-filled integrating sphere fitted with a JASCO FP-8600 spectrofluorometer.

B. Kinetic Monte Carlo simulations

For a comprehensive understanding of the efficiency loss processes, we performed three-dimensional kinetic Monte Carlo (KMC) simulations by using the algorithm implemented in the commercial software BUMBLEBEE [22, 26–33]. In this approach, the device is modeled as a collection of molecular sites arranged on a simple cubic grid with a lattice spacing of 1 nm. Each site may host an electron, a hole, a singlet exciton, or a triplet exciton and is, therefore, assigned an energy level for the ionization potential, electron affinity, singlet, and triplet energies. Injection layers are not explicitly modeled but a 0.2 eV energy barrier is positioned at both injecting electrodes. The charge transport is described as a hopping process using a Miller-Abrahams-type (MA) rate [31], with a wave function decay length for hopping of 0.3 nm and a nearest neighbor attempt-to-hop frequency of 3.33×10^{10} s^{-1} for both holes and electrons. A temperature of 293 K is assumed. Unlike previous studies [22,34], we found that a reduced electron mobility prefactor to model electron trapping in an effective way was unnecessary. Hence, we assumed equal hole and electron mobility parameters in all the materials. The decision to use the MA formalism is further supported by recent theoretical and KMC reports demonstrating that the Miller-Abrahams formalism is more appropriate for describing charge transport in amorphous organic semiconductor films than the Marcus formalism [35–37].

The software defines an exciton when a hole and an electron occupy the same molecular site. Its spin is determined probabilistically according to spin statistics, favoring a relative singlet-to-triplet probability of 1:3. Exciton formation is associated with an additional energy stabilization equal to the exciton binding energy. This is also taken into account as a further energy penalty when the hole or electron leaves the exciton site, thus causing the dissociation of the exciton. The energy levels considered in the KMC model are illustrated in Fig. 1. We do not explicitly consider the electronic character of each state (i.e., whether

it is of an intramolecular charge-transfer or a localized nature, or of an intermolecular CT or exciplex-like nature), yet we consider the spin. Excitonic processes are explicitly modeled, including the radiative and nonradiative decay of the singlet and triplet states, intersystem crossing (ISC), RISC, exciton diffusion, and losses resulting from interactions with polarons (exciton-polaron quenching) or other excitons (exciton-exciton annihilation). In exciton-exciton annihilation, the spin of the surviving exciton may or may not change, adhering to the spin conservation principle: singlet-singlet annihilation (SSA) results in a singlet, singlet-triplet annihilation (STA) results in a triplet, and triplet-triplet annihilation (TTA) results in either a singlet or triplet with a relative probability of 1:3. Exciton-polaron quenching and exciton-exciton annihilation processes are treated as on-site processes. Exciton diffusion, quenching, and annihilation phenomena are introduced via both the Dexter and Förster mechanisms, as discussed in Sec. S1 of the Supplemental Material [32] (including Refs. [22,26–30,32,34,38,39]).

The KMC simulations help to identify the processes occurring within the device [22,26,28,29,40]. However, this necessitates precise knowledge of the energy levels of the materials, or more specifically, their relative energy offsets and energetic disorder. The IP and EA values depicted in Fig. 1 were determined through a methodology involving the fabrication and characterization of unipolar hole-only and electron-only devices, in conjunction with the KMC simulations (for details regarding parameter refinement, see Sec. S1 of the Supplemental Material) [32]. In brief, we based the initial IP values for all the materials, except 2PTZBN, on literature values derived from photoelectron spectroscopy data. For 2PTZBN, we used cyclic voltammetry values as initial estimates due to the absence of photoelectron spectroscopy data [41]. We then estimated the EA values by adding the optical gap plus the singlet exciton binding energy to the IP values. We used a singlet exciton binding energy of 1.0 eV for all the materials, except for mCBP-CN, DMAC-TRZ, and 2PTZBN, where we used a value of 0.7 eV due to the intramolecular charge-transfer character of their lowest singlet states [42,43]. These binding energy values are consistent with an inverse photoemission spectroscopy study by Yoshida *et al.* [44], and similar values have also been used in other related studies [22,34,45]. To adjust for the impact of the local environment, we refined these starting values for the IP and EA values of each material by running the KMC simulations for hole-only and electron-only devices with these IP and EA values. The current density-voltage curves obtained from the KMC were compared with those obtained experimentally (Figs. S1–S8 in the Supplemental Material [32]), and the IP and EA values were adjusted until good agreement was obtained. This procedure is further detailed in the Secs. S1.1 and S1.2 in the Supplemental Material [32] (including Refs. [22,32,34,41–48]).

TABLE I. Material-specific parameters used for the KMC simulations. When two values are indicated for the same material, the literature value (left-hand side) is compared with the refined value (right-hand side).

	α-NPD		mCBP		mCBP-CN		DMAC-TRZ		TTPA	2PTZBN		T2T
E_{IP} [eV]	−5.40 [7]	−5.475[a]	−6.00[34]	−5.925[a]	−6.25 [49]		−5.80 [50]		−5.50 [7]	−5.19 [41]	−5.59[a]	−6.50 [34]
E_{EA} [eV]	−1.52[b]		−1.63[b]		−2.24[b]	−2.305[a]	−2.40[b]	−2.46[a]	−2.10[b]	−2.73 [41]	−2.33[a]	−1.94[b] −1.875[a]
E_S [eV]	3.12 [51]		3.37 [34]		3.31[d]		2.71[d]		2.46[d]	2.50[d]		3.56 [52]
E_T[eV]	2.38 [51]		2.90 [34]		2.78[d]		2.63[d]		1.60 [53]	2.37[d]		2.80 [52]
$k_{R,S}$, $k_{NR,S}$ [s^{-1}]	10^8, 10^8 [c]		10^8, 10^8 [c]		2.1×10^7 [d], 0[e]		2.2×10^7 [d], 0[e]		3.9×10^7 [d], 0[e]	3.4×10^7 [d], 0[e]		10^8, 10^8 [c]
k_{ISC} [s^{-1}]	0[c]		0[c]		10^8 [c]		4.0×10^7 [d]		6.6×10^7 [d]	1.9×10^7 [d]		0[c]
k_{RISC} [s^{-1}]	0[c]		0[c]		0[c]		1.5×10^6 [d]		0[c]	2.9×10^5 [d]		0[c]
$k_{R,T}$, $k_{NR,T}$ [s^{-1}]	0, 10^4 [c]		0, 10^4 [c]		0, 10^4 [c]		0[e], 7.3×10^4 [d]		0, 10^4 [c]	0[e], 4.6×10^4 [d]		0, 10^4 [c]

[a]Refined value, see Sec. III B in the main text and Sec. S1 in the Supplemental Material [32] for details.
[b]Estimated from the IP value, singlet energy (E_S), and assumed singlet exciton binding energy, see Sec. III B in the main text and Sec. S1 in the Supplemental Material [32] for more details.
[c]BUMBLEBEE default (assumed) value.
[d]Measured or derived value, see Sec. S2 in the Supplemental Material [32] for more details.
[e]Assumed in the fitting of experimental data, see Sec. S2 in the Supplemental Material [32].

Table I summarizes both the initial and final obtained values for IP and EA of this procedure. Note that this method is not guaranteed to produce the most correct absolute IP and EA values, yet we expect it to yield very reliable values relative to each other for the set of materials investigated.

Furthermore, we required excitonic parameters, including singlet and triplet energies, as well as photophysical rate constants such as radiative and nonradiative decay rates of singlet and triplet states, ISC rate, and RISC rate. We obtained these parameters through time-resolved spectroscopy on films (refer to Sec. S2 and Figs. S12–S14 in the Supplemental Material) [32] (including Refs. [54,55]). The spectroscopic data are also summarized in Table I and essentially match the literature values [41,43,49,56,57].

III. RESULTS AND DISCUSSION

A. Electrical and optical characterization

We first aim to investigate the impact of the RISC in the terminal emitter on efficiency loss processes in the OLEDs with a type-II-like energy level alignment between sensitizer and terminal emitter. For this, we fabricated OLEDs with the emissive layer sandwiched between hole injection/transport layers and an electron transport layer. Figure 1 shows the schematic layer structure of the OLED stack under investigation (refer to Sec. II A for the fabrication details and chemical names). For the emissive layer, we chose mCBP-CN as the host matrix. The host matrix is doped with DMAC-TRZ, serving as the TADF sensitizer, which enables percolative hole and electron transport, provided it is added at 10% or more [58]. The combination of mCBP-CN with DMAC-TRZ is a well-studied workhorse; it is known that no intermolecular state forms between them [16,56,58]. The chemical structures of EML materials are shown in Fig. 1.

We tested two different terminal emitters for HF-OLEDs based on a type-II-H-like level alignment. The first is a common fluorescent emitter, i.e., TTPA, henceforth referred to as the non-MR emitter [7,57,59]. Since triplet generation on the terminal emitter plays a crucial role in governing the efficiency loss processes in OLEDs, we also tested a second terminal emitter, 2PTZBN, which is itself a TADF emitter and has a narrow emission spectrum due to its MR character. We refer to it as the MR emitter. Both TTPA and 2PTZBN have similar ionization potentials ($E_{\mathrm{IP,TTPA}} = -5.50$ eV and $E_{\mathrm{IP,2PTZBN}} = -5.59$ eV) and a similar optical gap ($S_{1,\mathrm{TTPA}} = 2.46$ eV and $S_{1,\mathrm{2PTZBN}} = 2.50$ eV); the key difference is that the non-MR emitter TTPA does not exhibit RISC, while the MR emitter 2PTZBN does, with a rate of $k_{\mathrm{RISC}} = 2.9 \times 10^5$ s^{-1}, as determined from the transient PL measurements (Supplemental Material [32], Sec. S2). TTPA is used as the terminal emitter in HF-non-MR OLEDs, while 2PTZBN is used as the terminal emitter in HF-MR OLEDs.

TABLE II. Device nomenclature and emissive layer composition. Device names and the respective concentration of mCBP-CN, DMAC-TRZ, TTPA, and 2PTZBN in the emissive layer of these devices.

Device name	mCBP-CN (host)	DMAC-TRZ (sensitizer)	TTPA (non-MR)	2PTZBN (MR)
host-only	100%	–	–	–
ref-TADF	90%	10%	–	–
ref-non-MR	99%	–	1%	–
HF-non-MR	89%	10%	1%	–
ref-MR	99%	–	–	1%
HF-MR	89%	10%	–	1%

We also considered the following reference OLEDs to assess the influence of the respective omitted components: (i) a reference TADF OLED, comprising a mCBP-CN matrix with TADF emitter DMAC-TRZ (10 wt %) and no terminal emitter, (ii) a reference non-MR OLED, comprising an mCBP-CN matrix without TADF sensitizer but with the non-MR emitter (1 wt %), and (iii) a reference MR OLED, comprising an mCBP-CN matrix without TADF sensitizer but with the MR emitter (1 wt %). The combinations and concentrations of host, sensitizer, and terminal emitter studied as EMLs in this study, along with the corresponding device nomenclature, are summarized in Table II.

Before considering the OLEDs, some aspects of the hole- and electron-only devices merit closer examination and discussion. Figure 2 shows the current density-voltage (J–V) characteristics of the hole- and electron-only devices for various emissive layer compositions including host-only, ref-TADF, HF-non-MR, and HF-MR configurations (see Table II for host, sensitizer, and terminal emitter combinations and concentrations in the EML). Upon doping with 10 wt % DMAC-TRZ, both the hole and electron currents in ref-TADF devices decrease compared with the host-only devices. This aligns with recent findings on varied DMAC-TRZ:mCBP-CN concentration ratios in the emissive layer [58]. It implies that at a concentration of 10 wt % DMAC-TRZ or higher, transport primarily occurs via the DMAC-TRZ sites. Consequently, the host material's contribution to charge transport is minimal. Hence, importantly, the critical factors influencing charge dynamics within the emissive layer of HF-OLEDs are the IP and EA offsets between the TADF sensitizer and the terminal emitter.

Moreover, doping with either terminal emitter results in decreased electron and hole currents (Fig. 2). Specifically, the reduction in hole current is more pronounced with 1 wt % TTPA (HF-non-MR device) compared with 1 wt % 2PTZBN (HF-MR device), implying lower (less negative) ionization potentials for both TTPA and 2PTZBN relative to DMAC-TRZ, with TTPA acting as a deeper hole

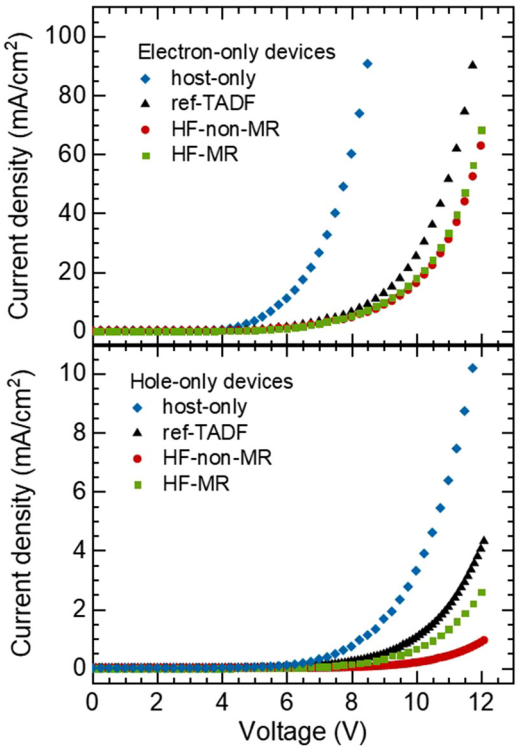

FIG. 2. Unipolar device characteristics. J–V characteristics of (top) the electron-only devices and (bottom) the hole-only devices for host-only, ref-TADF, HF-non-MR, and HF-MR devices. Refer to Table II for details on device nomenclature and emissive layer composition.

trap. Conversely, the electron current decreases similarly for both terminal emitters, which we attribute to dilution effects caused by a dopant with a lower (less negative) electron affinity than DMAC-TRZ [60]. We ruled out the possibility that the terminal emitters act as electron traps (see Figs. S20 and S21 in the Supplemental Material [32]). For this, the terminal emitter would need to have more negative electron affinities than the DMAC-TRZ. However, considering the ionization potentials and optical gaps detailed in Table I, such low electron affinities would imply unrealistically low exciton binding energies for a luminescent compound. Hence, the electron affinity of DMAC-TRZ sets a lower bound. Note that the charges are primarily transported by the DMAC-TRZ sites, which are 10 wt % of the total sites. A terminal emitter concentration of 0.5–5 wt %, hence, implies a relative trap and barrier concentration of 5–50%. Therefore, from our analysis of single carrier devices, we conclude that, indeed, both terminal emitters form type-II heterojunctions with the sensitizer DMAC-TRZ.

With this information, we can now consider the HF-OLEDs. Figure 3(a) presents the EQE-current density (EQE-J) curves for the ref-TADF OLED, ref-non-MR fluorescent OLED, and HF-non-MR OLED. Comparing OLEDs with and without the non-MR terminal emitter, i.e., the ref-TADF (10 wt % DMAC-TRZ and mCBP-CN) and HF-non-MR (1 wt % TTPA, 10 wt % DMAC-TRZ, and mCBP-CN) OLEDs, it is evident that adding the non-MR emitter TTPA introduces additional loss channels. Omitting the TADF sensitizer to create the ref-non-MR (1 wt % TTPA and mCBP-CN) fluorescent OLED results in an even worse performance. Figure 3(b) depicts the electroluminescence (EL) spectra of the ref-TADF and HF-non-MR OLEDs. The EL of the HF-non-MR OLED exhibits some contribution from the TADF sensitizer DMAC-TRZ, consistent with a Förster radius for the energy transfer from DMAC-TRZ to TTPA of 2.1 nm (Fig. S15 in the Supplemental Material [32]). Increasing the concentration of TTPA from 0.5 to 1 to 2 to 5 wt %, decreases the contribution of DMAC-TRZ emission in the EL spectra (Fig. S16 in the Supplemental Material [32]). However, the EQE also decreases due to a significant build-up of triplet population on the non-MR fluorescent emitter TTPA with its increased concentration (Fig. S16 in the Supplemental Material [32]). In the ref-non-MR OLED, an additional emission peak centered around 450 nm is observed, which is absent in the ref-TADF and HF-non-MR OLEDs. This peak likely originates from recombination at the interface with the hole transport layer, as it does not correspond to emission from either the host or the non-MR emitter (see Fig. S12 in the Supplemental Material [32]), and the devices are electron-dominated. This additional peak is suppressed when the TADF sensitizer is added, as charge transport then occurs primarily via percolation on the sensitizer itself.

Figure 3(c) presents the EQE-current density (EQE-J) curves for the ref-TADF (10 wt % DMAC-TRZ and mCBP-CN) OLED, ref-MR (1 wt % 2PTZBN and mCBP-CN) OLED, and HF-MR (1 wt % 2PTZBN, 10 wt % DMAC-TRZ, and mCBP-CN) OLED. Considering the two reference OLEDs, ref-TADF OLED exhibits higher EQE and lower roll-off in comparison with ref-MR OLED, attributed to a lower RISC rate in 2PTZBN compared with DMAC-TRZ ($2.9 \times 10^5\ s^{-1}$ vs $1.5 \times 10^6\ s^{-1}$). On the other hand, comparing OLEDs with and without the MR terminal emitter, i.e., ref-TADF and HF-MR OLEDs, suggests that adding the MR terminal emitter maintains peak EQE. This is in contrast to the case of HF-non-MR OLEDs, emphasizing the advantageous effect of utilizing a terminal emitter that also demonstrates RISC, effectively mitigating loss processes associated with triplets. The benefits of triplet harvesting on 2PTZBN become more apparent when considering that, unlike HF-non-MR OLEDs, the EQE of HF-MR OLEDs remains similar as the 2PTZBN concentration increases from 0.5 to 1 to 2 wt %, dropping significantly only when the concentration is further increased to 5 wt % (Fig. S17 in the Supplemental Material [32]). Nevertheless, the HF-MR OLEDs still exhibit slightly increased roll-off compared with the ref-TADF OLEDs

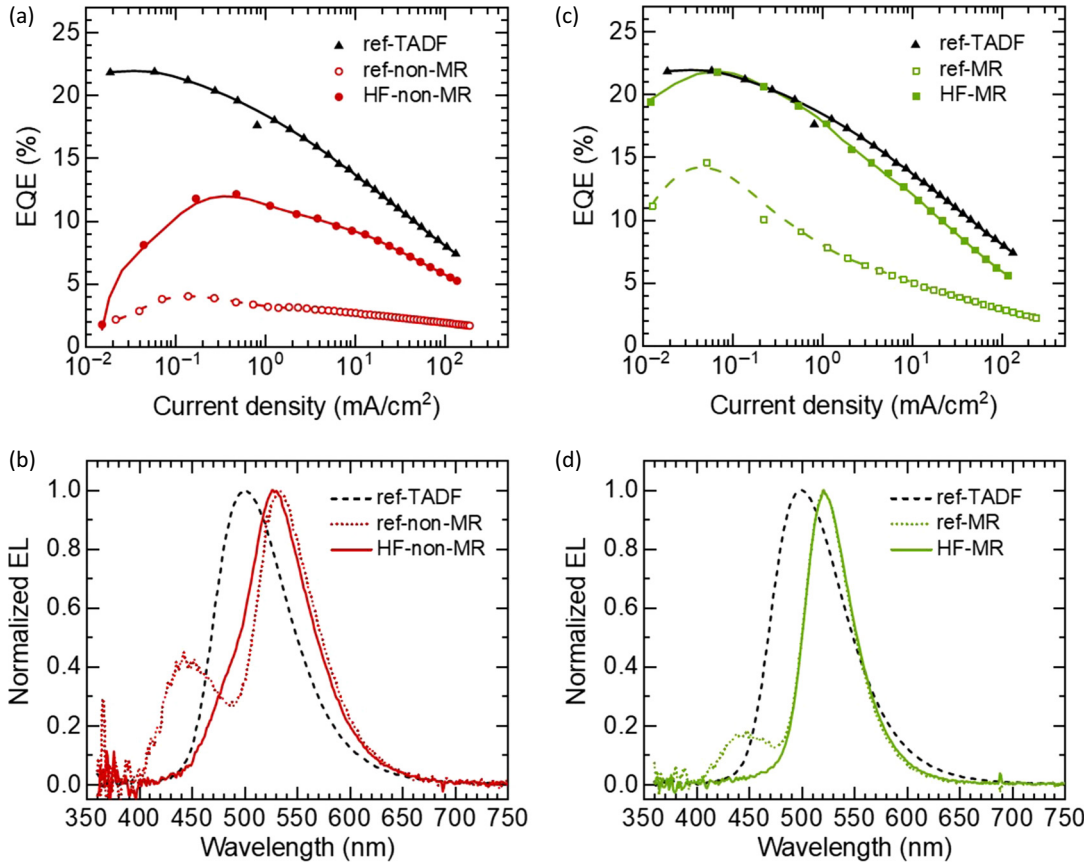

FIG. 3. OLED characteristics. (a) EQE as a function of current density (EQE-J curves) and (b) electroluminescence spectra for the ref-TADF, ref-non-MR, and HF-non-MR OLEDs. (c) EQE-J curves and (d) electroluminescence spectra for the ref-TADF, ref-MR, and HF-MR OLEDs.

at higher current densities, which is further examined in Sec. IV B. Moreover, the narrow EL spectrum of HF-MR OLED, corresponding to the 2PTZBN emission spectrum (Figs. S15 and S25 in the Supplemental Material [32]), contrasts with the broader emission spectra of the ref-TADF OLED [Fig. 3(d)]. Analogous to the case of the HF-non-MR OLED, omitting the sensitizer in the ref-HF-MR OLED results in the appearance of an additional peak around 450 nm, which is presumably due to recombination at the interface with the hole transport layer.

B. Efficiency loss processes

To identify what is causing the losses, we combined the electronic parameters optimized via KMC with the excitonic parameters determined through spectroscopy to simulate the bipolar devices. Figure 4 shows a comparison between the experimentally measured and simulated J–V characteristics and EQE-J curves for the ref-TADF (10 wt % DMAC-TRZ and mCBP-CN), HF-non-MR (1 wt % TTPA, 10 wt % DMAC-TRZ, and mCBP-CN), and HF-MR (1 wt % 2PTZBN, 10 wt % DMAC-TRZ, and mCBP-CN) OLEDs, demonstrating a satisfactory agreement in all cases. Limitations in KMC statistics at low current density prevented us from running simulations at current densities below 0.2–0.3 mA cm^{-2}. We calculated the external quantum efficiency (EQE) as the product of the internal quantum efficiency and a constant 33% light outcoupling efficiency. This choice is based on the previously reported emitter orientation factor for DMAC-TRZ doped in mCBP-CN [46,61]. Minor discrepancies between the experimentally measured and simulated EQE data may, therefore, result from differences in outcoupling efficiency across devices. Additionally, changes in the emission profile within the EML as a function of current density, an effect not accounted for in our modeling, could further contribute to these differences.

In both HF systems, electron-hole recombination primarily occurs on the TADF sensitizer DMAC-TRZ sites, followed by energy transfer to terminal emitter sites. Consistent with our observations on the energy level alignment of materials in Sec. IV A, significant hole density is present on both DMAC-TRZ and terminal emitter sites, while electrons predominantly accumulate on DMAC-TRZ sites (see Figs. S20 and S21 in the Supplemental Material [32]), thus determining exciton generation.

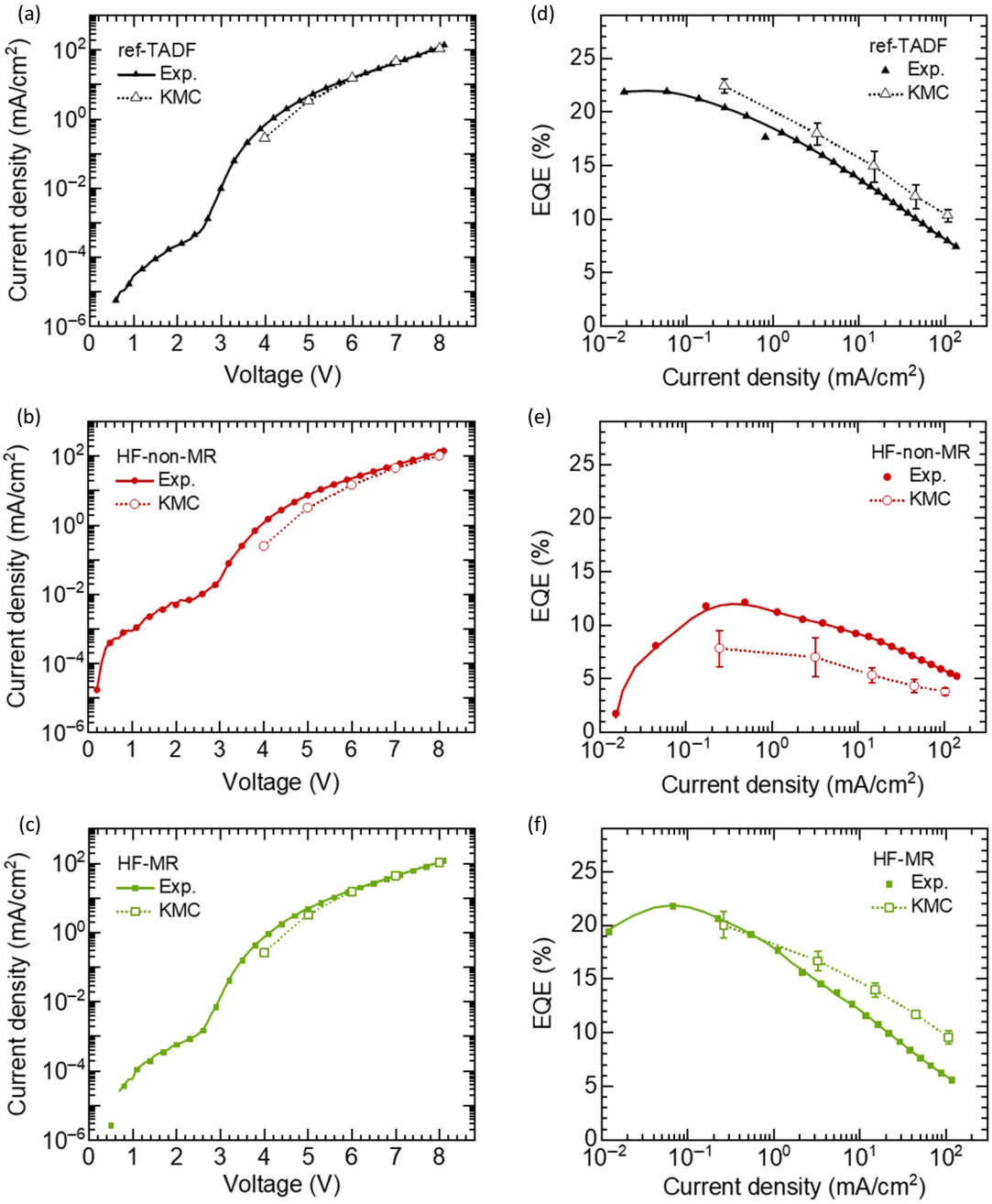

FIG. 4. Comparison of experimental and simulation data. J–V characteristics of the (a) ref-TADF, (b) HF-non-MR, and (c) HF-MR OLEDs. EQE-J curves of the (d) ref-TADF, (e) HF-non-MR, and (f) HF-MR OLEDs. Experimental data (solid symbol and solid line) and the data obtained from the KMC simulations (open symbols) are shown. Dotted lines serve as a guide to the eye for the simulation data. The error bars are calculated as the standard deviation of the current density or EQE over the simulation replicates. In (a)–(c), the error bars for the simulated current density are smaller than the symbol size.

With KMC results at hand, we can analyze the impact of each kind of loss process in the three devices. Figures 5(a)–5(c) present simulation results depicting the relative contributions of various excitonic processes to the efficiency roll-off observed in ref-TADF, HF-non-MR, and HF-MR OLEDs. At low current densities (e.g., 3 mA/cm^2), we observe merely triplet nonradiative decay (gray) and exciton-polaron quenching (shades of blue) across all the devices, while exciton-exciton annihilation (yellow and orange) starts contributing significantly at higher current densities (e.g., 45 mA/cm^2).

We attribute the significant exciton-polaron quenching in all the devices to charge imbalance within the EML, which arises due to a difference of 0.45 eV in the ionization

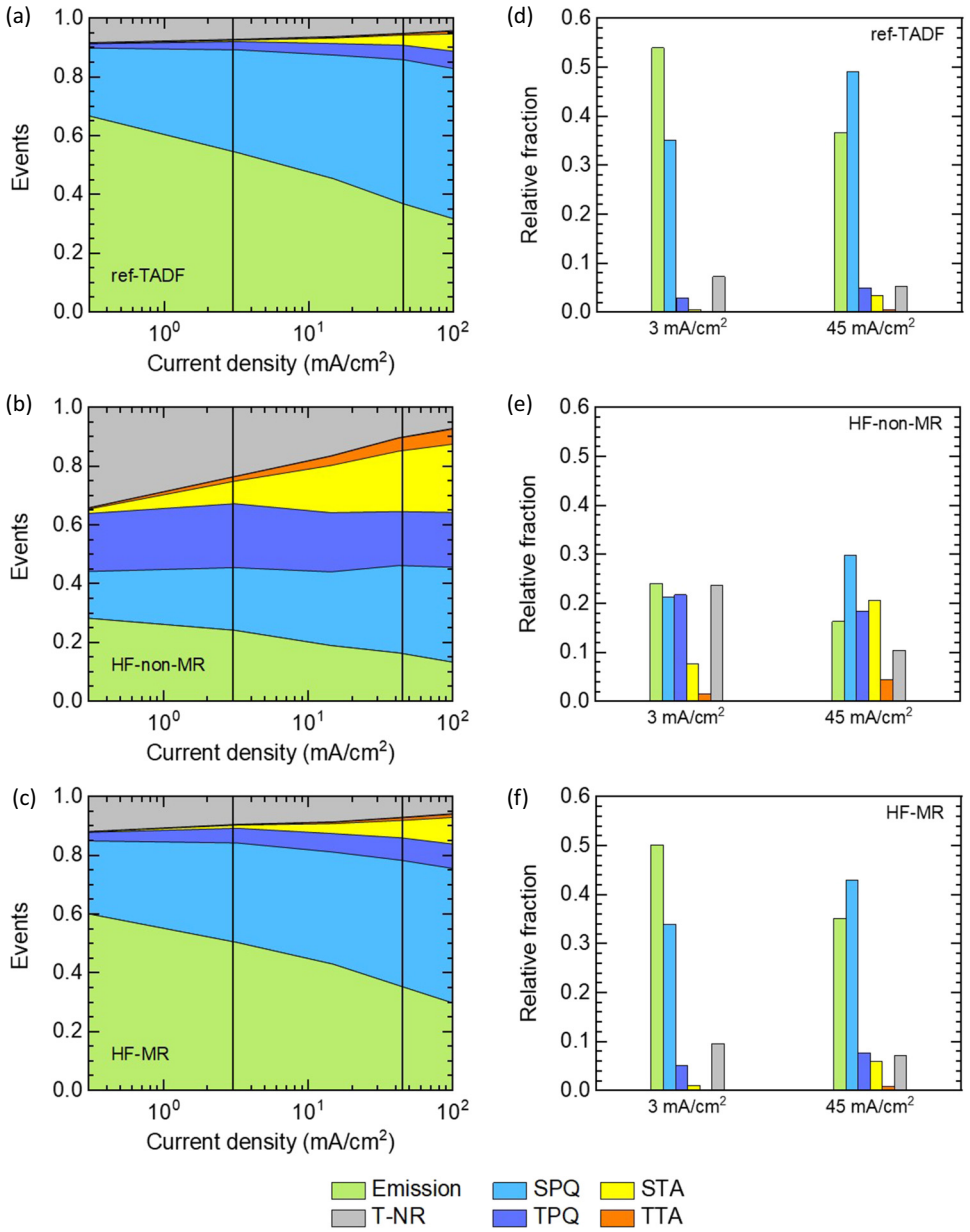

FIG. 5. Efficiency loss processes. The relative contributions of the different excitonic processes that occur are shown as a function of current density for the (a) ref-TADF, (b) HF-non-MR, and (c) HF-MR OLEDs. The different excitonic processes include singlet emission, singlet-polaron quenching, singlet-triplet annihilation, triplet nonradiative decay, triplet-polaron quenching, and triplet-triplet annihilation. The reference lines at 3 mA/cm^2 and 45 mA/cm^2 in (a)–(c) indicate the current densities at which the contributions of different excitonic processes to the overall efficiency loss are compared in the (d) ref-TADF, (e) HF-non-MR, and (f) HF-MR OLEDs.

potential between α-NPD and mCBP (Fig. 1 and Table I). At the interface between the α-NPD:mCBP mixed layer and the pure mCBP layer, the higher ionization potential of mCBP produces an energy barrier that hinders hole transport. This hindrance leads to an unbalanced charge distribution in the EML, reducing recombination efficiency and leaving an excess of free electrons, which can effectively quench excitons on both the sensitizer and terminal emitters (see Sec. S3 in the Supplemental Material for a further discussion [32]).

Let us briefly discuss the nature of the annihilation processes. From the simulated singlet and triplet exciton profiles [panels (c) and (d) in Figs. S18, S20, and S21 in the Supplemental Material [32]], we observe that the triplet density is one to two orders of magnitude higher than the singlet density in all the devices. Therefore, we argue

that, in all three devices, the most relevant annihilation process for singlet excitons is Förster-mediated singlet-triplet annihilation (STA), as the singlet density is too low to yield a significant amount of singlet-singlet annihilation (SSA). Similarly, triplet excitons are more likely to undergo Dexter-mediated triplet-triplet annihilation (TTA) than triplet-singlet annihilation. The relatively high fraction of STA (compared with TTA) can be explained by the long-range nature of Förster interactions, which favor the STA loss pathway despite the low singlet density. In contrast, TTA is hindered by the short-range nature of Dexter interactions, despite the higher triplet density. We recall that, in our devices, triplets predominantly localize on the terminal emitters (see Figs. S20 and S21 in the Supplemental Material [32]) at a concentration of only 1%.

When comparing the efficiency loss processes between the ref-TADF OLED [Fig. 5(a)] and HF-non-MR OLED [Fig. 5(b)], the HF-non-MR OLED shows higher contributions from triplet-related loss processes, such as triplet-polaron quenching (TPQ), STA, and TTA [as quantified in Fig. S22 in the Supplemental Material [32], Figs. 5(d) and 5(e)]. We attribute this increase to the increased triplet accumulation on the non-MR fluorescent emitter TTPA (Fig. S20 in the Supplemental Material [32]), which does not exhibit RISC and, thus, has a long triplet lifetime.

When comparing the efficiency loss processes in the ref-TADF OLED [Fig. 5(a)] and the HF-MR OLED [Fig. 5(c)], we observe similarities and differences. Both OLEDs show strikingly similar profiles where singlet-polaron quenching is the dominant loss process, with increased contributions from TPQ and STA at higher current densities. At 45 mA/cm^2, the HF-MR OLED exhibits slightly higher contributions from TPQ and STA compared with the ref-TADF OLED [as quantified in Fig. S22 in the Supplemental Material [32], Figs. 5(d) and 5(f)]. We attribute this to a slower RISC rate on the MR emitter 2PTZBN compared with the TADF sensitizer DMAC-TRZ. This slower RISC rate likely causes the higher roll-off of the HF-MR OLED compared with the ref-TADF OLED, as shown in Fig. 2(c). This finding may also explain the higher efficiency roll-off observed in MR-emitter-based HF-OLEDs compared with ref-TADF OLEDs in other related studies [13,16,17].

C. Role of intermolecular states

We now address the formation and role of intermolecular states in type-II architecture-based HF-OLEDs. In a type-II-like alignment between the TADF sensitizer and terminal emitter, the energy level alignment allows excitons to dissociate into geminate pairs on neighboring sites, leading to the creation of an intermolecular CT or exciplex state through the loss of an exciton. To better understand this further loss mechanism, we examine the energetics involved. We define the "IS-S_1 offset" as the energy difference between the sensitizer-terminal emitter intermolecular state and the lowest singlet state, which in a HF-OLED is the terminal emitter singlet state. The formation and population of the IS is favorable if the IS-S_1 offset is negative (type-II-L) and unfavorable if the IS-S_1 offset is positive (type-II-H), as displayed in Fig. 1. For our molecules, the IS forms with a hole residing on a terminal emitter site and an electron residing on a nearby TADF sensitizer site. As outlined previously [22,62], we estimate the IS energy (E_{IS}) according to

$$E_{\mathrm{IS}} = E_{\mathrm{EA,\,sensitizer}} - E_{\mathrm{IP,TE}} - E_b, \tag{1}$$

i.e., based on the electron affinity of the sensitizer ($E_{\mathrm{EA,\,sensitizer}}$) and the ionization potential ($E_{\mathrm{IP,\,TE}}$) of each terminal emitter (detailed in Table S2 in the Supplemental Material [32]), plus a Coulomb interaction term acting as the intermolecular state binding energy (E_b). In our KMC model, we use an intersite distance of 1 nm and a dielectric constant of 3, which results in a binding energy of 0.48 eV for the intermolecular state. The resulting IS energies are then 2.56 eV and 2.65 eV for the HF-non-MR and HF-MR OLEDs, respectively (see Table S2 in the Supplemental Material [32]). Comparing these values with the experimentally determined singlet energies of the non-MR terminal emitter TTPA (2.46 eV) and the MR terminal emitter 2PTZBN (2.50 eV), we find that the IS-S_1 offset in HF-non-MR and HF-MR OLEDs is approximately 100 and 150 meV, respectively. A summary of these energy levels is presented in Figs. 6(a) and 7(a) for HF-non-MR and HF-MR OLEDs, respectively.

Of course, the statistical variation in the intermolecular distances and orientations implies a Gaussian distribution of these energies rather than sharp values. Moreover, there are also intermolecular states from nonnearest-neighbor sites, as well as intermolecular states formed between any combination of the host, TADF sensitizer, and terminal emitter (see Table S2 in the Supplemental Material [32] for relevant intermolecular state energies). These effects are explicitly considered in the KMC simulations and, hence, in the results presented in Figs. 4–7. The values quoted in our discussion pertain to the mean value of the distribution from nearest-neighbor sensitizer-terminal emitter intermolecular states, which is sufficient to grasp the essential physics of the system and to explain the observed behavior of the OLEDs.

To investigate the impact of the intermolecular state formation on efficiency loss in hyperfluorescent OLEDs, we conducted KMC simulations of hypothetical "model" HF-OLEDs. The configuration of these model devices was kept identical to that of "pristine" HF-OLEDs (Fig. 1). However, in these model devices, we disfavored intermolecular state formation by having the highest possible IS-S_1 offset, which can be obtained when the IP

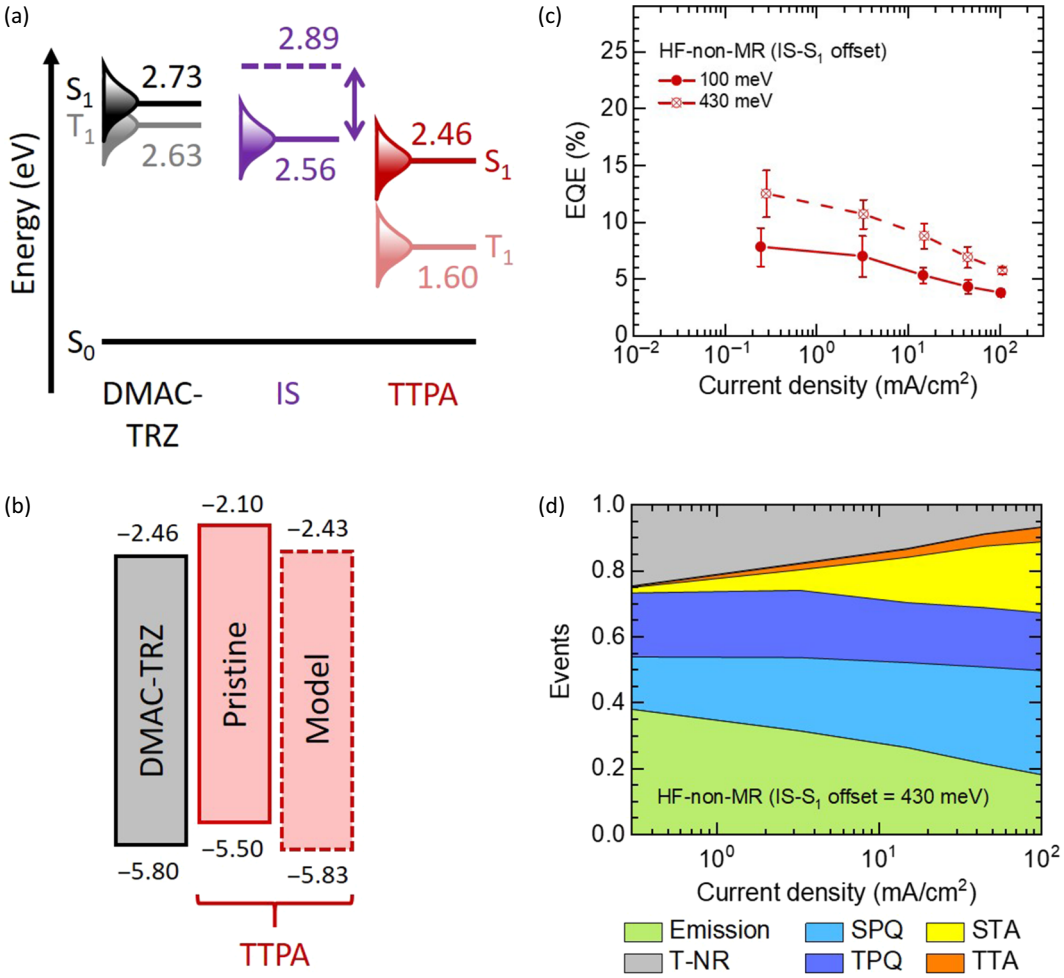

FIG. 6. Impact of the intermolecular state formation on efficiency loss in the HF-non-MR OLEDs. (a) Singlet and triplet energies for DMAC-TRZ (black) and TTPA (red). The TTPA (hole) and DMAC-TRZ (electron) intermolecular state energy is shown in purple for the pristine (solid line) and the model (dashed line) HF-non-MR OLEDs. The IS-S_1 offset, defined as the energy difference between the intermolecular state and TTPA singlet energy, is 100 meV for the pristine and 430 meV for the model HF-non-MR OLEDs. (b) A schematic illustration of the ionization potential and electron affinity of TTPA in the pristine and model HF-non-MR OLEDs. (c) Simulated EQE-J curves for the pristine (IS-S_1 offset = 100 meV) and the model (IS-S_1 offset = 430 meV) HF-non-MR OLEDs. (d) Relative contribution of various excitonic processes to the overall efficiency loss in the model HF-non-MR OLED.

and EA values of the terminal emitter and sensitizer are equal. To achieve this, we shifted both the IP and EA of the terminal emitter to lower energies, such that $E_{\mathrm{IP,TE}}{}^{\mathrm{model}} = E_{\mathrm{IP,TE}}{}^{\mathrm{pristine}} + \Delta_{\mathrm{TE}}$ and likewise for EA. The shift was $\Delta_{\mathrm{TTPA}} = -0.33$ eV for TTPA [Fig. 6(b)] and $\Delta_{\mathrm{2PTZBN}} = -0.18$ eV for 2PTZBN [Fig. 7(b)]. Although the IP and EA values of the sensitizer and terminal emitter are not exactly equal after the shift, the IP and EA offsets between the sensitizer and terminal emitter are less than ±30 meV [see Figs. 6(b) and 7(b)], which is comparable to the room temperature thermal energy. To maintain consistency in the electronic parameters between the pristine and model devices, while still ensuring a high IS–S_1 offset to suppress IS formation, it was not considered essential to exactly match the IP and EA values of the sensitizer and terminal emitter. Doing so would have required independently adjusting the IP and EA of the terminal emitters, which would in turn alter their IP–EA gap. Moreover, we emphasize that lowering the energy levels further would result in the formation of the reverse intermolecular states (type II-L), with holes on the sensitizer and electrons on the terminal emitter. A comparison of the energy levels in pristine and model devices is displayed in Figs. 6(b) and 7(b) for HF-non-MR and HF-MR OLEDs, respectively. All the other simulation parameters, as per the simulation results shown in Figs. 4 and 5, remain unchanged. We note that the simulations implicitly take into account that, for this energy level arrangement, the formation of an intermolecular state between the sensitizer and the terminal emitter is less likely than the occurrence of energy transfer.

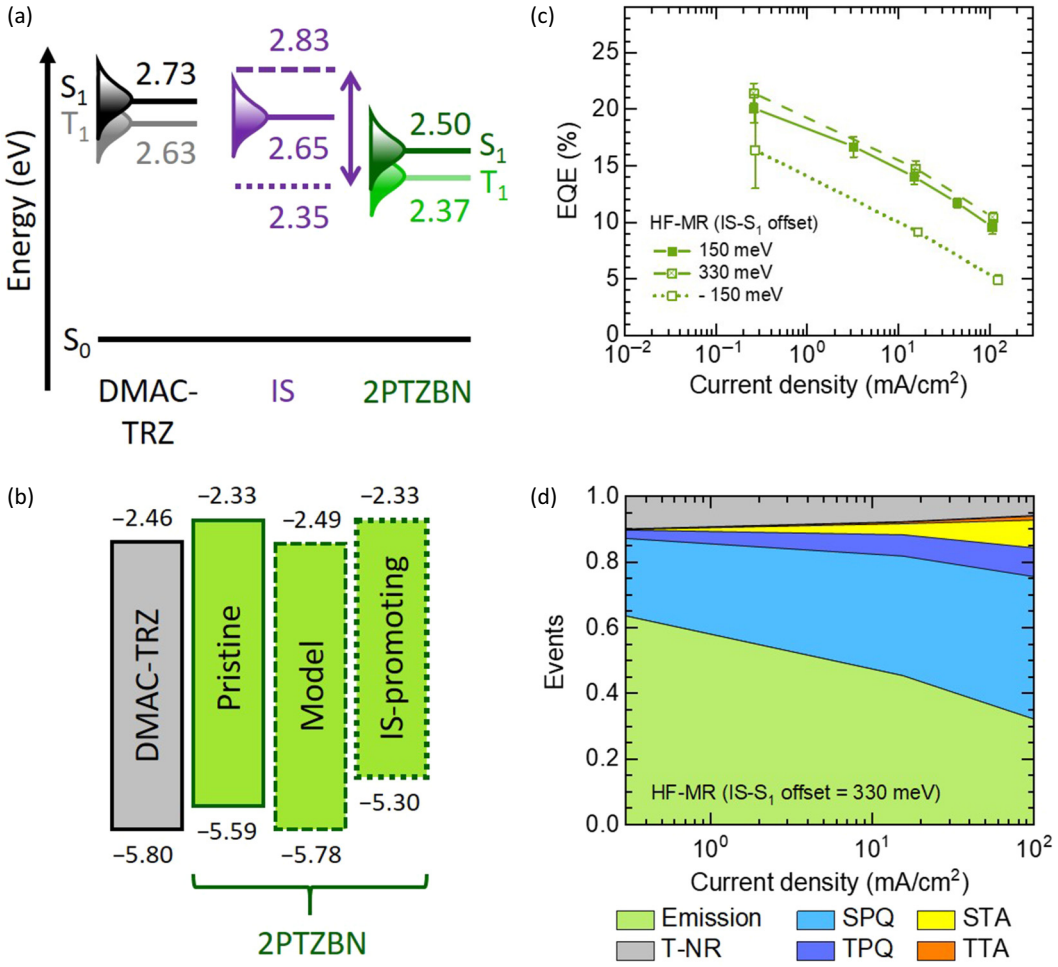

FIG. 7. Impact of the intermolecular state formation on efficiency loss in the HF-MR OLEDs. (a) Singlet and triplet energies for DMAC-TRZ (black) and 2PTZBN (green). The 2PTZBN (hole) and DMAC-TRZ (electron) intermolecular state energy is shown in purple for the pristine (solid line), model (dashed line), and IS-promoting (dotted line) HF-MR OLEDs. The IS-S_1 offset, defined as the energy difference between the intermolecular state and 2PTZBN singlet energy, is 150 meV for the pristine, 330 meV for the model, and −150 meV for the IS-promoting HF-MR OLEDs. (b) A schematic illustration of the ionization potential and electron affinity of 2PTZBN in the pristine, model, and IS-promoting HF-MR OLEDs. (c) Simulated EQE-J curves for the pristine (IS-S_1 offset = 150 meV), model (IS-S_1 offset = 330 meV), and IS-promoting (IS-S_1 offset = −150 meV) HF-MR OLEDs. (d) Relative contribution of various excitonic processes to the overall efficiency loss in the model HF-MR OLED.

In Figs. 6 and 7, we compare the simulated EQE-J curve and the efficiency roll-off between the model devices and their pristine counterparts. Let us first analyze the HF-non-MR OLEDs. As shown in Fig. 6(a), the IS-S_1 offset in pristine and model HF-non-MR OLED is approximately 100 and 430 meV, respectively, with the latter being the purposefully designed maximum IS-S_1 offset. We expect that model devices will not exhibit any efficiency loss due to intermolecular state formation and dissociation. Therefore, it provides a benchmark to test whether the pristine HF-non-MR OLED with an IS-S_1 offset of 100 meV is effective in preventing losses arising from intermolecular state formation and dissociation. As illustrated in Fig. 6(c), the peak EQE of the model and the pristine OLEDs are about 12% and 8%, respectively, reducing to 6% and 4% at 100 mA/cm^2 due to roll-off. This implies that the pristine, i.e., the real OLED, obtains only about two-thirds of the maximum possible efficiency, suggesting that significant losses may occur due to exciton dissociation into an intermolecular state, followed by either its separation into free charges or its nonradiative decay [63]. This strong effect may be surprising, yet it is worth recalling that one needs to consider not only the formation and thermal population of the intermolecular state 100 meV above the terminal emitter singlet state, but also the fact that the density of state (DOS) of the intermolecular state is disorder-broadened into a Gaussian shape with a standard deviation of about 50–100 meV. Hence, in particular, the tail states of the

DOS of the intermolecular state can be populated easily and, thus, act as particularly active dissociation sites (type II-H in Fig. 1).

The relative contributions of various excitonic processes to the efficiency roll-off observed in the model HF-non-MR OLED, as depicted in Fig. 6(d), mirror those of the pristine HF-non-MR OLED in Fig. 5(b). However, model OLEDs exhibit a reduction in triplet-related quenching processes, such as TPQ, STA, TTA, and nonradiative triplet decay, as quantified in Fig. S23 in the Supplemental Material [32], and thus emission is more likely. We consider that, in the pristine OLED, charges resulting from exciton dissociation may recombine again and, as a result, increase the triplet concentration.

We next consider the impact of the IS-S_1 offset in pristine and model HF-MR OLEDs. The maximum offset that can be obtained for our system by minimizing the IP difference and EA difference is 330 meV [Figs. 7(a) and 7(b)]. This compares against the IS-S_1 offset of 150 meV in the pristine system. As illustrated in Fig. 7(c), the model HF-MR OLED shows only a 1–2% enhancement in peak EQE compared with the pristine HF-MR OLED, i.e., they are equivalent within the device performance error, implying that intermolecular state dissociation does not play a role in the HF-MR OLED with an IS-S_1 offset of 150 meV. This is further confirmed by the negligible difference in the relative contributions of various excitonic processes to the efficiency roll-off observed in the pristine and model HF-MR OLEDs [c.f., Figs. 5(c) versus 7(d), further quantified in Fig. S23 in the Supplemental Material [32]].

To summarize, if we compare the HF-non-MR OLED and the HF-MR OLED, we find that in the HF-non-MR OLED, there is an IS-S_1 offset of 100 meV that is insufficient to suppress intermolecular state formation and population, subsequent dissociation, and recombination to the triplet state. In contrast, in the HF-MR OLED with an IS-S_1 offset of 150 meV, intermolecular state formation and population, dissociation, and increased triplet formation are not an issue. The difference between the two systems is the IS-S_1 offset of 100 meV against 150 meV, and the non-MR versus the MR nature of the terminal emitter. We would expect a slightly larger IS-S_1 offset in the HF-MR OLED to perhaps reduce any intermolecular state-related effects, yet not to eliminate them entirely. We, therefore, attribute the disappearance of the intermolecular state-related losses to the important role played by RISC in the MR emitter. This reasoning is further supported by the negligible change in the EQE-J curve when the IS–S_1 offset in the HF-MR OLED is reduced from 150 to 100 meV (Fig. S24 in the Supplemental Material [32]). We argue as follows. The intermolecular state-related losses in the HF-non-MR OLED ultimately stem from increased triplet accumulation on TTPA. Due to the absence of RISC, it acts as a triplet trap. In the HF-MR OLED with the MR terminal emitter, even if there is an increased (transient) formation of triplet states from intermolecular state formation, dissociation, and recombination, such triplets are converted back into singlets due to their sufficient RISC rate.

Naturally, the question arises: Is RISC all we need? To check this, we simulated an IS-promoting device where, as illustrated in Fig. 7(b), by keeping the electron affinity of 2PTZBN unaltered while shifting the ionization potential such that $E_{\mathrm{IP,TE}}{}^{\mathrm{IS-promoting}} = E_{\mathrm{IP,TE}}{}^{\mathrm{pristine}} + 0.30$ eV, a negative IS-S_1 offset of -150 meV results. As shown in Fig. 7(c), the IS-promoting HF-MR OLED is only about 70% efficient compared with the pristine HF-MR OLED. Evidently, if the additional amount of triplet state created through the intermolecular state formation and dissociation becomes too large, the RISC rate no longer suffices to remove them. It then becomes an issue of the relative rates of additional triplet formation versus conversion into singlets. Thus, we can conclude that RISC alone is not sufficient to eliminate the losses associated with intermolecular state formation and dissociation: a positive IS-S_1 offset is required first of all. Having RISC on the terminal emitter, however, mitigates the losses further.

IV. CONCLUSIONS

In summary, our experiments show that the HF-non-MR OLED with the non-MR fluorescent terminal emitter shows lower EQE compared with the reference TADF OLED. In contrast, the HF-MR OLED employing the MR terminal emitter achieves comparable peak EQE to the reference TADF OLED. However, it exhibits slightly higher roll-off, attributed to slower RISC in the MR emitter relative to the TADF sensitizer. The KMC simulations identify triplet-polaron quenching and singlet-triplet annihilation as primary contributors to this roll-off difference.

Our study of intermolecular state formation and dissociation in HF-OLEDs with type-II heterojunction-like alignment between the TADF sensitizer and terminal emitter highlights strategies for minimizing losses. We find that intermolecular state formation results in efficiency loss. We attribute this loss to the intermolecular state dissociation, followed by recombination in a statistical singlet-triplet ratio, ultimately leading to an increased triplet population on the terminal emitter. This loss channel can be significantly suppressed if the intermolecular state energy is at least 150 meV above the singlet energy of the terminal emitter. This requires a suitable choice of the relative ionization potential and electron affinity levels of the terminal emitter and TADF sensitizer. When the intermolecular state energy falls below this threshold, partial suppression persists but it is limited by the disorder-broadened DOS in the amorphous films. Residual triplet-related losses, including triplet-polaron quenching, singlet-triplet annihilation, and triplet nonradiative decay, can be further mitigated by using terminal emitters with

RISC, such as MR emitters. Ultimately, it is essential that the RISC rate of the terminal emitter is higher than the rate of additional triplet state population resulting from the formation of any intermolecular state.

ACKNOWLEDGMENTS

The authors acknowledge funding through the EU Marie Skłodowska-Curie Innovative Training Network "TADFsolutions" (Grant No. 101073045) and "TADFlife" (Grant No. 812872). R.S. and A.K. also acknowledge the funding from Deutsche Forschungsgemeinschaft (Grant No. KO3973/8-1). R.S. would like to thank Andrei Stankevych, Andrey Kadashchuk, and Sergey Bagnich for useful discussions.

R.S. conceived the project. R.S. and K.S. conducted device fabrication and characterization. R.S. and L.G.F. carried out photophysical measurements. G.C. performed the KMC simulations with inputs from R.S. and E.T. A.P.M., S.G., and A.K. supervised group members involved in the project. R.S., G.C. and A.K. wrote the manuscript with inputs from all the authors.

DATA AVAILABILITY

The data that support the findings of this article are not publicly available upon publication because it is not technically feasible and/or the cost of preparing, depositing, and hosting the data would be prohibitive within the terms of this research project. The data are available from the authors upon reasonable request.

[1] M. A. Baldo, D. F. O'Brien, Y. You, A. Shoustikov, S. Sibley, M. E. Thompson, and S. R. Forrest, Highly efficient phosphorescent emission from organic electroluminescent devices, Nature **395**, 151 (1998).

[2] H. Uoyama, K. Goushi, K. Shizu, H. Nomura, and C. Adachi, Highly efficient organic light-emitting diodes from delayed fluorescence, Nature **492**, 234 (2012).

[3] U. Monkowius and H. Yersin. Complexes with small singlet-triplet energy separations for use in opto-electronic components (singlet harvesting effect). DE 10 2008 033 563 A1, 2008.

[4] A. Endo, M. Ogasawara, A. Takahashi, D. Yokoyama, Y. Kato, and C. Adachi, Thermally activated delayed fluorescence from Sn(4+)-porphyrin complexes and their application to organic light emitting diodes–a novel mechanism for electroluminescence, Adv. Mater. **21**, 4802 (2009).

[5] A. Monkman, Why do we still need a stable long lifetime deep blue OLED emitter?, ACS Appl. Mater. Interfaces **14**, 20463 (2022).

[6] T. Hatakeyama, K. Shiren, K. Nakajima, S. Nomura, S. Nakatsuka, K. Kinoshita, J. Ni, Y. Ono, and T. Ikuta, Ultrapure blue thermally activated delayed fluorescence molecules: Efficient HOMO-LUMO separation by the multiple resonance effect, Adv. Mater. **28**, 2777 (2016).

[7] H. Nakanotani, T. Higuchi, T. Furukawa, K. Masui, K. Morimoto, M. Numata, H. Tanaka, Y. Sagara, T. Yasuda, and C. Adachi, High-efficiency organic light-emitting diodes with fluorescent emitters, Nat. Commun. **5**, 4016 (2014).

[8] H. Abroshan, Y. Zhang, X. Zhang, C. Fuentes-Hernandez, S. Barlow, V. Coropceanu, S. R. Marder, B. Kippelen, and J. L. Brédas, Thermally activated delayed fluorescence sensitization for highly efficient blue fluorescent emitters, Adv. Funct. Mater. **30**, 2005898 (2020).

[9] J. Adachi, H. Kakizoe, P. K. D. Tsang, and A. Endo, 10.1: Invited paper: Hyperfluorescence™; a game changing technology of OLED display, SID Symp. Dig. Tech. Pap. **50**, 95 (2019).

[10] T. Furukawa, H. Nakanotani, M. Inoue, and C. Adachi, Dual enhancement of electroluminescence efficiency and operational stability by rapid upconversion of triplet excitons in OLEDs, Sci. Rep. **5**, 8429 (2015).

[11] Y. Wada, H. Nakagawa, S. Matsumoto, Y. Wakisaka, and H. Kaji, Organic light emitters exhibiting very fast reverse intersystem crossing, Nat. Photonics **14**, 643 (2020).

[12] Y. Gawale, R. Ansari, K. R. Naveen, and J. H. Kwon, Forthcoming hyperfluorescence display technology: relevant factors to achieve high-performance stable organic light emitting diodes, Front. Chem. **11**, 1211345 (2023).

[13] K. R. Naveen, P. Palanisamy, M. Y. Chae, and J. H. Kwon, Multiresonant TADF materials: triggering the reverse intersystem crossing to alleviate the efficiency roll-off in OLEDs, Chem. Commun. **59**, 3685 (2023).

[14] C.-Y. Chan, M. Tanaka, Y.-T. Lee, Y.-W. Wong, H. Nakanotani, T. Hatakeyama, and C. Adachi, Stable pure-blue hyperfluorescence organic light-emitting diodes with high-efficiency and narrow emission, Nat. Photonics **15**, 203 (2021).

[15] S. O. Jeon, K. H. Lee, J. S. Kim, S.-G. Ihn, Y. S. Chung, J. W. Kim, H. Lee, S. Kim, H. Choi, and J. Y. Lee, High-efficiency, long-lifetime deep-blue organic light-emitting diodes, Nat. Photonics **15**, 208 (2021).

[16] K. Stavrou, L. G. Franca, A. Danos, and A. P. Monkman, Key requirements for ultraefficient sensitization in hyperfluorescence organic light-emitting diodes, Nat. Photonics **18**, 554 (2024).

[17] K. Stavrou, S. Madayanad Suresh, D. Hall, A. Danos, N. A. Kukhta, A. M. Z. Slawin, S. Warriner, D. Beljonne, Y. Olivier, A. Monkman, *et al.*, Emission and absorption tuning in TADF B,N-doped heptacenes: Toward ideal-blue hyperfluorescent OLEDs, Adv. Opt. Mater. **10**, 2200688 (2022).

[18] A. Köhler and H. Bässler, *Electronic Processes in Organic Semiconductors: An Introduction* (John Wiley & Sons, Weinheim, 2015).

[19] Y. T. Lee, C. Y. Chan, M. Tanaka, M. Mamada, U. Balijapalli, Y. Tsuchiya, H. Nakanotani, T. Hatakeyama, and C. Adachi, Investigating HOMO energy levels of terminal emitters for realizing high-brightness and stable TADF-assisted fluorescence organic light-emitting diodes, Adv. Electron. Mater. **7**, 2001090 (2021).

[20] K. Stavrou, A. Danos, T. Hama, T. Hatakeyama, and A. Monkman, Hot vibrational states in a high-performance multiple resonance emitter and the effect of excimer

quenching on organic light-emitting diodes, ACS Appl. Mater. Interfaces **13**, 8643 (2021).

[21] J. J. M. Halls, J. Cornil, D. A. dos Santos, R. Silbey, D.-H. Hwang, A. B. Holmes, J. L. Brédas, and R. H. Friend, Charge- and energy-transfer processes at polymer/polymer interfaces: A joint experimental and theoretical study, Phys. Rev. B **60**, 5721 (1999).

[22] S. Gottardi, M. Barbry, R. Coehoorn, and H. van Eersel, Efficiency loss processes in hyperfluorescent OLEDs: A kinetic Monte Carlo study, Appl. Phys. Lett. **114**, 073301 (2019).

[23] M. Deussen, M. Scheidler, and H. Bässler, Electric field-induced photoluminescence quenching in thin-film light emitting diodes based on poly(phenyl-p-phenylene vinylene), Synth. Met. **73**, 123 (1995).

[24] S. Haneder, E. Da Como, J. Feldmann, M. M. Rothmann, P. Strohriegl, C. Lennartz, O. Molt, I. Münster, C. Schildknecht, and G. Wagenblast, Effect of electric field on coulomb-stabilized excitons in host/guest systems for deep-blue electrophosphorescence, Adv. Funct. Mater. **19**, 2416 (2009).

[25] C. Murawski, K. Leo, and M. C. Gather, Efficiency roll-off in organic light-emitting diodes, Adv. Mater. **25**, 6801 (2013).

[26] R. Coehoorn, H. van Eersel, P. Bobbert, and R. Janssen, Kinetic Monte Carlo study of the sensitivity of OLED efficiency and lifetime to materials parameters, Adv. Funct. Mater. **25**, 2024 (2014).

[27] A. Ligthart, X. de Vries, L. Zhang, M. C. W. M. Pols, P. A. Bobbert, H. van Eersel, and R. Coehoorn, Effect of triplet confinement on triplet–triplet annihilation in organic phosphorescent host–guest systems, Adv. Funct. Mater. **28**, 1804618 (2018).

[28] M. Mesta, H. van Eersel, R. Coehoorn, and P. A. Bobbert, Kinetic Monte Carlo modeling of the efficiency roll-off in a multilayer white organic light-emitting device, Appl. Phys. Lett. **108**, 133301 (2016).

[29] H. van Eersel, P. A. Bobbert, R. A. J. Janssen, and R. Coehoorn, Monte Carlo study of efficiency roll-off of phosphorescent organic light-emitting diodes: Evidence for dominant role of triplet-polaron quenching, Appl. Phys. Lett. **105**, 143303 (2014).

[30] H. van Eersel, P. A. Bobbert, and R. Coehoorn, Kinetic Monte Carlo study of triplet-triplet annihilation in organic phosphorescent emitters, J. Appl. Phys. **117**, 115502 (2015).

[31] F. Yang, H. van Eersel, J. Wang, Q. Niu, P. A. Bobbert, R. Coehoorn, F. Liu, and G. Zhou, Dilution-induced current-density increase in disordered organic semiconductor devices: A kinetic Monte Carlo study, Phys. Rev. Appl. **21**, 014050 (2024).

[32] See Supplemental Material at http://link.aps.org/supplemental/10.1103/k967-sr56 for parameter optimization (Sec. S1), photophysical data (Sec. S2), discussion on the effect of the co-evaporated α-NPD:mCBP (1:1) layer (Sec. S3), further OLED results (Sec. S4), further simulation results (Sec. S5), further photophysical data (Sec. S6), and energies of the CT states between different materials (Sec. S7).

[33] Bumblebee is currently provided by SCM, Amsterdam, The Netherlands, https://www.scm.com/oled/oled-workflows.

[34] C. Hauenstein, S. Gottardi, E. Torun, R. Coehoorn, and H. van Eersel, Identification of OLED degradation scenarios by kinetic Monte Carlo simulations of lifetime experiments, Front. Chem. **9**, 823210 (2021).

[35] X. de Vries, P. Friederich, W. Wenzel, R. Coehoorn, and P. A. Bobbert, Full quantum treatment of charge dynamics in amorphous molecular semiconductors, Phys. Rev. B **97**, 075203 (2018).

[36] R. Saxena, T. Meier, S. Athanasopoulos, H. Bässler, and A. Köhler, Kinetic Monte Carlo study of triplet-triplet annihilation in conjugated luminescent materials, Phys. Rev. Appl. **14**, 034050 (2020).

[37] R. Saxena, V. R. Nikitenko, I. I. Fishchuk, Y. V. Burdakov, Y. V. Metel, J. Genoe, H. Bässler, A. Köhler, and A. Kadashchuk, Role of the reorganization energy for charge transport in disordered organic semiconductors, Phys. Rev. B **103**, 165202 (2021).

[38] P. K. Watkins, A. B. Walker, and G. L. B. Verschoor, Dynamical Monte Carlo modelling of organic solar cells: The dependence of internal quantum efficiency on morphology, Nano Lett. **5**, 1814 (2005).

[39] M. Mesta, M. Carvelli, R. J. de Vries, H. van Eersel, J. J. van der Holst, M. Schober, M. Furno, B. Lussem, K. Leo, P. Loebl, *et al.*, Molecular-scale simulation of electroluminescence in a multilayer white organic light-emitting diode, Nat. Mater. **12**, 652 (2013).

[40] Y. Shen and N. C. Giebink, Monte Carlo simulations of nanoscale electrical inhomogeneity in organic light-emitting diodes and its impact on their efficiency and lifetime, Phys. Rev. Appl. **4**, 054017 (2015).

[41] T. Hua, L. Zhan, N. Li, Z. Huang, X. Cao, Z. Xiao, S. Gong, C. Zhou, C. Zhong, and C. Yang, Heavy-atom effect promotes multi-resonance thermally activated delayed fluorescence, Chem. Eng. J. **426**, 131169 (2021).

[42] A. Stankevych, R. Saxena, J. Grüne, S. Lulei, A. Sperlich, S. Athanasopoulos, A. Vakhnin, P. Sahay, W. Brütting, V. Dyakonov, *et al.*, Charge-carrier photogeneration in single-component organic carbazole-based semiconductors via low excitation power triplet-triplet annihilation, Phys. Rev. Appl. **20**, 064029 (2023).

[43] T. A. Lin, T. Chatterjee, W. L. Tsai, W. K. Lee, M. J. Wu, M. Jiao, K. C. Pan, C. L. Yi, C. L. Chung, K. T. Wong, *et al.*, Sky-blue organic light emitting diode with 37% external quantum efficiency using thermally activated delayed fluorescence from spiroacridine-triazine hybrid, Adv. Mater. **28**, 6976 (2016).

[44] H. Yoshida and K. Yoshizaki, Electron affinities of organic materials used for organic light-emitting diodes: A low-energy inverse photoemission study, Org. Electron. **20**, 24 (2015).

[45] M. Hasan, S. Saggar, A. Shukla, F. Bencheikh, J. Sobus, S. K. M. McGregor, C. Adachi, S. C. Lo, and E. B. Namdas, Probing polaron-induced exciton quenching in TADF based organic light-emitting diodes, Nat. Commun. **13**, 254 (2022).

[46] B. A. Naqvi, M. Schmid, E. Crovini, P. Sahay, T. Naujoks, F. Rodella, Z. Zhang, P. Strohriegl, S. Brase, E. Zysman-Colman, *et al.*, What controls the orientation of TADF emitters?, Front. Chem. **8**, 750 (2020).

[47] A. Stankevych, R. Saxena, A. Vakhnin, F. May, N. Kinaret, D. Andrienko, J. Genoe, H. Bässler, A. Köhler, and

A. Kadashchuk, Monitoring the charge-carrier-occupied density of states in disordered organic semiconductors under nonequilibrium conditions using thermally stimulated luminescence spectroscopy, Phys. Rev. Appl. **19**, 054007 (2023).

[48] A. Stankevych, A. Vakhnin, D. Andrienko, L. Paterson, J. Genoe, I. Fishchuk, H. Bässler, A. Köhler, and A. Kadashchuk, Density of states of OLED host materials from thermally stimulated luminescence, Phys. Rev. Appl. **15**, 044050 (2021).

[49] S. G. Ihn, N. Lee, S. O. Jeon, M. Sim, H. Kang, Y. Jung, D. H. Huh, Y. M. Son, S. Y. Lee, M. Numata, *et al.*, An alternative host material for long-lifespan blue organic light-emitting diodes using thermally activated delayed fluorescence, Adv. Sci. (Weinh) **4**, 1600502 (2017).

[50] Y. Wada, K. Shizu, S. Kubo, T. Fukushima, T. Miwa, H. Tanaka, C. Adachi, and H. Kaji, Highly efficient solution-processed host-free organic light-emitting diodes showing an external quantum efficiency of nearly 18% with a thermally activated delayed fluorescence emitter, Appl. Phys. Express **9**, 032102 (2016).

[51] V. Jankus, C. J. Chiang, F. Dias, and A. P. Monkman, Deep blue exciplex organic light-emitting diodes with enhanced efficiency; P-type or E-type triplet conversion to singlet excitons?, Adv. Mater. **25**, 1455 (2013).

[52] H.-F. Chen, S.-J. Yang, Z.-H. Tsai, W.-Y. Hung, T.-C. Wang, and K.-T. Wong, 1,3,5-Triazine derivatives as new electron transport–type host materials for highly efficient green phosphorescent OLEDs, J. Mater. Chem. **19**, 8112 (2009).

[53] H. Abroshan, V. Coropceanu, and J.-L. Brédas, Hyperfluorescence-based emission in purely organic materials: Suppression of energy-loss mechanisms via alignment of triplet excited states, ACS Mater. Lett. **2**, 1412 (2020).

[54] D. Sun, E. Duda, X. Fan, R. Saxena, M. Zhang, S. Bagnich, X. Zhang, A. Köhler, and E. Zysman-Colman, Thermally activated delayed fluorescent dendrimers that underpin high-efficiency host-free solution-processed organic light-emitting diodes, Adv. Mater. **34**, 2110344 (2022).

[55] D. Sun, R. Saxena, X. Fan, S. Athanasopoulos, E. Duda, M. Zhang, S. Bagnich, X. Zhang, E. Zysman-Colman, and A. Köhler, Regiochemistry of donor dendrons controls the performance of thermally activated delayed fluorescence dendrimer emitters for high efficiency solution-processed organic light-emitting diodes, Adv. Sci. (Weinh) **9**, 2201470 (2022).

[56] K. Stavrou, L. G. Franca, and A. P. Monkman, Photophysics of TADF guest-host systems: Introducing the idea of hosting potential, ACS Appl. Electron. Mater. **2**, 2868 (2020).

[57] Y.-H. Yu, C.-H. Huang, J.-M. Yeh, and P.-T. Huang, Effect of methyl substituents on the N-diaryl rings of anthracene-9,10-diamine derivatives for OLEDs applications, Org. Electron. **12**, 694 (2011).

[58] S. Sem, S. Jenatsch, P. Sahay, S. Züfle, M. Schmid, W. Brütting, and B. Ruhstaller, Detailed electro-optical modeling of thermally-activated delayed fluorescent OLEDs with different host-guest concentrations, Org. Electron. **107**, 106553 (2022).

[59] T. Higuchi, H. Nakanotani, and C. Adachi, High-efficiency white organic light-emitting diodes based on a blue thermally activated delayed fluorescent emitter combined with green and red fluorescent emitters, Adv. Mater. **27**, 2019 (2015).

[60] T. A. Madison, A. G. Gagorik, and G. R. Hutchison, Charge transport in imperfect organic field effect transistors: Effects of charge traps, J. Phys. Chem. C **116**, 11852 (2012).

[61] A. Hofmann, M. Schmid, and W. Brütting, The many facets of molecular orientation in organic optoelectronics, Adv. Opt. Mater. **9**, 2101004 (2021).

[62] A. Ligthart, T. D. G. Nevels, C. H. L. Weijtens, P. A. Bobbert, and R. Coehoorn, Mechanistic description of the efficiency loss in organic phosphorescent host–guest systems due to triplet-polaron quenching, Org. Electron. **91**, 106058 (2021).

[63] J. Benduhn, K. Tvingstedt, F. Piersimoni, S. Ullbrich, Y. Fan, M. Tropiano, K. A. McGarry, O. Zeika, M. K. Riede, C. J. Douglas, *et al.*, Intrinsic nonradiative voltage losses in fullerene-based organic solar cells, Nat. Energy **2**, 17053 (2017).